Title

Elastocaloric signatures of symmetric and antisymmetric strain-tuning of quadrupolar and magnetic phases in DyB2C2.

Journal

Proceedings of the National Academy of Sciences of USA, 120(35)

Authors

Fisher, Ian

Ye, Linda

Sun, Yue

et al.

Publication Date

2023-08-29

DOI

10.1073/pnas.2302800120

Peer reviewed

PNAS RESEARCH ARTICLE | PHYSICS

Elastocaloric signatures of symmetric and antisymmetric strain-tuning of quadrupolar and magnetic phases in DyB_2C_2

Linda Ye[a,b,1], Yue Sun[c,d], Veronika Sunko[c,d], Joaquin F. Rodriguez-Nieva[e], Matthias S. Ikeda[a,b], Thanapat Worasaran[a,b], Matthew E. Sorensen[a,e], Maja D. Bachmann[a,b], Joseph Orenstein[c,d], and Ian R. Fisher[a,b,1]

Edited by John Tranquada, Brookhaven National Laboratory, Upton, NY; received February 17, 2023; accepted July 22, 2023

The adiabatic elastocaloric effect measures the temperature change of a given system with strain and provides a thermodynamic probe of the entropic landscape in the temperature-strain space. Here, we demonstrate that the DC bias strain-dependence of AC elastocaloric effect allows decomposition of the latter into symmetric (rotation-symmetry-preserving) and antisymmetric (rotation-symmetry-breaking) strain channels, using a tetragonal *f*-electron intermetallic DyB_2C_2—whose antiferroquadrupolar order breaks local fourfold rotational symmetries while globally remaining tetragonal—as a showcase example. We capture the strain evolution of its quadrupolar and magnetic phase transitions using both singularities in the elastocaloric coefficient and its jumps at the transitions, and the latter we show follows a modified Ehrenfest relation. We find that antisymmetric strain couples to the underlying order parameter in a biquadratic (linear-quadratic) manner in the antiferroquadrupolar (canted antiferromagnetic) phase, which are attributed to a preserved (broken) global tetragonal symmetry, respectively. The broken tetragonal symmetry in the magnetic phase is further evidenced by elastocaloric strain-hysteresis and optical birefringence. Additionally, within the staggered quadrupolar order, the observed elastocaloric response reflects a quadratic increase of entropy with antisymmetric strain, analogous to the role magnetic field plays for Ising antiferromagnetic orders by promoting pseudospin flips. Our results demonstrate AC elastocaloric effect as a compact and incisive thermodynamic probe into the coupling between electronic degrees of freedom and strain in free energy, which holds the potential for investigating and understanding the symmetry of a wide variety of ordered phases in broader classes of quantum materials.

antisymmetric strain | quadrupolar order | elastocaloric effect | strongly correlated electron systems

Strain—and the associated modification of lattice parameters—has long been used as a highly effective means to tune material properties, particularly in the context of hydrostatic pressure (1). Recent developments of piezoelectric-based devices capable of applying uniaxial stress to materials in a nearly continuous fashion, have highlighted the unique roles that anisotropic strain can play (2–4). Its application in strongly correlated electron systems where competing phases are expected to be sensitively tuned by external control parameters (5) opens up particularly exciting possibilities; in this context, the potential of anisotropic strain as an effective tuning parameter has begun to be demonstrated for a number of superconducting (3, 4, 6, 7), nematic (7, 8), and charge density wave states (9–11). Uniaxial stress, like hydrostatic pressure, couples to these phases by modifying the atomic spacing in the lattice hosts; however, an important difference between the two as material tuning parameters is that hydrostatic pressure should, in principle, preserve the space group symmetry, whereas strain induced by uniaxial stress can modify the space group with relatively small lattice distortions.

Whether and how the generated lattice deformation conforms to the symmetries of the pristine crystal structure depends on how strain/stress is implemented in given experiments. In this context, group theoretical irreducible representations provide a basis to decompose an arbitrary infinitesimal deformation into a superposition of orthogonal modes categorized by how they transform under certain symmetry elements in the original, undeformed point group (12, 13). Once the system undergoes a phase transition, the spatial symmetry of the order parameter dictates the form of its coupling with the irreducible strain modes. This thus motivates the notion of symmetry decomposition that has been applied to a number of experimental strain studies in recent years: The critical temperatures of the superconducting transition in Sr_2RuO_4 (3) and the nematic transition in iron-based superconductors (8, 14) have been demonstrated to be tuned by strains belonging to different irreducible representations in highly distinct manners; categorizing strain-induced resistance changes (elastoresistance) also into

Significance

Characterizing the symmetries of ordered phases is paramount in the study of strongly correlated electron systems, and anisotropic lattice distortion/strain offer a fruitful avenue for probing and tuning these phases. Our experimental framework resolves symmetric (rotation–symmetry–preserving) and antisymmetric (rotation–symmetry–breaking) strain effects in free energy using a thermodynamic quantity, the elastocaloric effect. By tracing out the entropy landscape of an f-electron intermetallic in the temperature–strain plane, we demonstrate that the strain-even (odd) component of the elastocaloric response corresponds to symmetric (antisymmetric) lattice deformation modes distinctively coupled to the underlying electronic degrees of freedom. Along with the derived Ehrenfest relation, the elastocaloric effect has potential applications in placing experimental constraints on the spatial symmetry of wider classes of emergent phases in quantum materials.

The authors declare no competing interest.

This article is a PNAS Direct Submission.

[1]To whom correspondence may be addressed. Email: lindaye0@stanford.edu or irfisher@stanford.edu.

This article contains supporting information online at https://www.pnas.org/lookup/suppl/doi:10.1073/pnas.2302800120/-/DCSupplemental.

Published August 22, 2023.

irreducible representations allows the introduction of elastoresistance tensor (15), whose components in distinct symmetry channels enabled distinguishing different microscopic mechanisms of coupling between strain and conduction electrons (16–18). These works demonstrate that decomposing an applied strain into distinct symmetry channels provides an organizing principle toward a systematic understanding of experimentally obtained strain responses. This can be especially important for systems which undergo phase transitions with spatially anisotropic order parameters—examples include nematic, spin/charge density wave, orbital and multipolar orders.

In the present work, adding to the symmetry-resolving capabilities of anisotropic strain, we apply a symmetry-decomposition framework to a strain-based thermodynamic quantity, namely, the adiabatic elastocaloric coefficient. We employ this technique to unravel the interplay between symmetric (rotational–symmetry–preserving) and antisymmetric (rotational–symmetry–breaking) strains and the underlying anisotropic f-electron degrees of freedom in a tetragonal intermetallic DyB_2C_2. The localized f electrons in DyB_2C_2 are known to host an antiferroquadrupolar order at low temperature; here at each Dy site the local tetragonal symmetry is broken with time-reversal symmetry intact (this is characterized by a finite electrical quadrupolar moment), and the global tetragonal symmetry is retained by a staggered pattern of the quadrupolar moments along the c-axis (19). Locally resembling electronic nematicity, a considerable coupling is expected between antisymmetric strains that also breaks tetragonal symmetry with the local quadrupole moments (20), while how such coupling tunes a staggered order has not been experimentally determined. We therefore employ the symmetry resolution of the elastocaloric effect to investigate how the staggered anisotropic order is tuned in both symmetric and antisymmetric strain channels. Numerous other strongly correlated electron systems exhibit similar spatially modulated rotational–symmetry–breaking orders—such as orbital ordering in transition metal oxides (21, 22), spin and charge stripe order in the low temperature tetragonal phase in $La_{2-x}Ba_xCuO_4$ (23, 24), along with a few f electron-based "hidden order states" (25)—we anticipate the methodology demonstrated in our study to be potentially relevant for such systems.

The article is organized as follows: We first discuss the elastocaloric effect itself and its symmetry properties in Section ; in Sections and , we use the elastocaloric effect to categorize the symmetric and antisymmetric strain effects to the quadrupolar and magnetic phase transitions in the system; we then focus on the antisymmetric strain responses away from the phase transitions in Section and in Section discuss broader scopes of using the symmetry decomposition aspect of the elastocaloric effect as an experimental probe of spatially anisotropic orders and fluctuations.

Elastocaloric Effect and Its Symmetry Decomposition

The adiabatic elastocaloric coefficient is defined as the temperature T change of a given system in response to strain ϵ as $(\partial T/\partial \epsilon)_S$, and it has recently emerged as an incisive tool for the study of strain responses of a number of quantum materials (26, 27). In these studies, the elastocaloric coefficients are experimentally probed through the measurement of a temperature oscillation in response to an AC strain, at a frequency such that a quasi-adiabatic condition is achieved (26). To illustrate the physical origin of the elastocaloric effect, in Fig. 1*A* we depict with a thick two-headed arrow the thermodynamic trajectory of an AC elastocaloric measurement on a generic system in the T-ϵ phase space. As adiabatic processes are confined along the black solid isentropic contours, the normalized temperature oscillation (adiabatic elastocaloric coefficient) can be related to the ϵ-derivative of entropy S in the isothermal condition (26):

$$\left(\frac{\partial T}{\partial \epsilon}\right)_S = -\frac{T}{C_\epsilon}\left(\frac{\partial S}{\partial \epsilon}\right)_T. \qquad [1]$$

Here C_ϵ is the heat capacity at fixed ϵ. Eq. **1** implies that the elastocaloric effect can be in turn used to characterize the entropy landscape with ϵ. We note that strictly speaking strain ϵ_{ij} is a 3×3 tensor and in Eq. **1** we use ϵ to denote the experimentally generated linear combinations of ϵ_{ij} components; the ϵ-derivatives $(\partial T/\partial \epsilon)_S$ and $(\partial S/\partial \epsilon)_T$ are defined for all other components of ϵ_{ij} being held to zero. We return to the specific combination of strain tensor components shortly. Unlike transport-based strain derivatives such as elastoresistivity, whose interpretation requires an understanding of the conduction electron scattering processes (15), $(\partial T/\partial \epsilon)_S$ provides a direct thermodynamic probe into the coupling between strain and

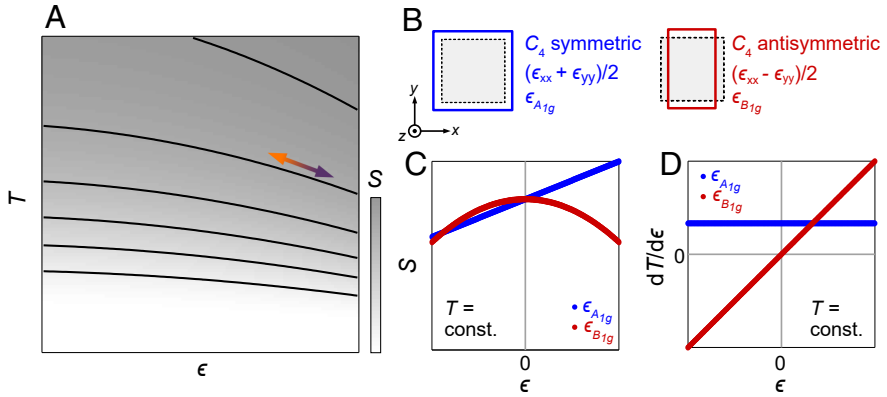

Fig. 1. Adiabatic elastocaloric effect and its symmetry properties. (*A*) Schematic of adiabatic AC elastocaloric effect in a temperature (T)-strain (ϵ) phase space, where the black solid lines are isentropic contours. The intensity of gray shade indicates the value of entropy S. The colored arrow illustrates the temperature oscillation induced by AC strain along the isentropic lines. (*B*) Schematic of $\frac{1}{2}(\epsilon_{xx}+\epsilon_{yy})$ ($\epsilon_{A_{1g}}$, blue box) and $\frac{1}{2}(\epsilon_{xx}-\epsilon_{yy})$ ($\epsilon_{B_{1g}}$, red box). The gray dashed box indicates an undeformed tetragonal lattice. (*C* and *D*) Schematic of the lowest-order evolution of S (*C*) and $dT/d\epsilon$ (*D*) with ϵ in the respective symmetric $\epsilon_{A_{1g}}$ (blue) and antisymmetric $\epsilon_{B_{1g}}$ (red) strain channels (see text).

underlying degrees of freedom in a given system in free energy (28). Eq. **1** further suggests that $(\partial T/\partial \epsilon)_S \cdot T^{-1}$, which we can extract from a single experiment, may be viewed as a Grüneisen parameter with respect to ϵ, Γ_ϵ, analogous to that defined in the context of hydrostatic pressure and magnetic field (27–30).

In the following, we lay out how spatial symmetry operations constrain the form of the elastocaloric coefficient $(\partial T/\partial \epsilon)_S$, using the fourfold rotational symmetry C_4 as an example. For a system with C_4 as one of its symmetry elements (we take z as the fourfold axis and assume that for simplicity, the system preserves inversion symmetry and mirror symmetry as well, forming the point group D_{4h}), the irreducible representations of strains are $\frac{1}{2}(\epsilon_{xx}+\epsilon_{yy})$, ϵ_{zz} (A_{1g}) and $\frac{1}{2}(\epsilon_{xx}-\epsilon_{yy})$ (B_{1g}), ϵ_{xy} (B_{2g}) and ϵ_{xz}, ϵ_{yz} (E_g). In the following, we restrict ourselves to normal strains and the shear strain components ϵ_{xz}, ϵ_{yz}, ϵ_{xy} are kept zero. In Fig. 1*B*, we contrast two of the in-plane strain modes $\frac{1}{2}(\epsilon_{xx}+\epsilon_{yy})$ and $\frac{1}{2}(\epsilon_{xx}-\epsilon_{yy})$, which belongs to A_{1g} and B_{1g} representations of D_{4h}, respectively; under a $\pi/2$-rotation ($x \to y, y \to -x$), the former is symmetric ($\frac{1}{2}(\epsilon_{xx}+\epsilon_{yy}) \to \frac{1}{2}(\epsilon_{xx}+\epsilon_{yy})$) while the latter is antisymmetric ($\frac{1}{2}(\epsilon_{xx}-\epsilon_{yy}) \to -\frac{1}{2}(\epsilon_{xx}-\epsilon_{yy})$). Since S as a scalar remains invariant under C_4, the lowest order allowed dependence of S on $\epsilon_{A_{1g}}(\epsilon_{B_{1g}})$ is linear (quadratic) in a Taylor expansion:

$$S = S^0 + S^{A^1_{1g}}\epsilon_{A_{1g}} + S^{A^2_{1g}}\epsilon^2_{A_{1g}} + S^{B^2_{1g}}\epsilon^2_{B_{1g}} + \ldots \qquad [2]$$

Here S^{X^i} are ϵ-independent coefficients for $\epsilon^i_X (X = A_{1g}, B_{1g})$ and in Eq. **2** we only enumerate up to quadratic terms. These contributions give $\partial T/\partial \epsilon$ the following form:

$$\left(\frac{\partial T}{\partial \epsilon}\right)_S = D^{A^0_{1g}} + D^{A^1_{1g}}\epsilon_{A_{1g}} + D^{B^1_{1g}}\epsilon_{B_{1g}} + \ldots, \qquad [3]$$

where D_{X^i} are ϵ-independent coefficients. From Eq. **3**, we see that an ϵ-independent, constant response in $(\partial T/\partial \epsilon)_S$ necessarily arise from $\epsilon_{A_{1g}}$, while an ϵ-linear contribution may either originate from $\epsilon_{A_{1g}}$ or $\epsilon_{B_{1g}}$.

In many material systems, Eqs. **2** and **3** may be further simplified via comparison with hydrostatic pressure experiments, which exclusively probe A_{1g} effects. In particular, the strain-dependence of critical temperature T_c of given phase transitions can often be regarded as an indicator of wider free energy landscape; when T_c evolves linearly with pressure, $\epsilon^2_{A_{1g}}$ terms in thermodynamic variables and $\epsilon_{A_{1g}}$-linear term in $(\partial T/\partial \epsilon)_S$ can reasonably be excluded for proximate regions in the ϵ–T plane.* Under such circumstances including the subject of this study (31), we may attribute the ϵ-quadratic and -linear components in S to antisymmetric and symmetric channels illustrated respectively in red and blue in Fig. 1*C*. The corresponding constant and ϵ-linear components of $(\partial T/\partial \epsilon)_S$ are illustrated in Fig. 1*D*. This suggests that by examining $(\partial T/\partial \epsilon)_S$ over an extended ϵ-range, the constant/linear (even/odd) responses of $dT/d\epsilon$ can be used to distinguish contributions from symmetric and antisymmetric strains. We note that as the out-of-plane mode ϵ_{zz} transforms identically with $\frac{1}{2}(\epsilon_{xx}+\epsilon_{yy})$ under C_4, the above arguments about $\frac{1}{2}(\epsilon_{xx}+\epsilon_{yy})$ also applies to ϵ_{zz}. Before applying this constant/linear criterion to our experimental observations, we note that we have adopted a number of assumptions here, including 1) that the different symmetry channels are independent (i.e. higher-order terms like $\epsilon_{A_{1g}}\epsilon^2_{B_{1g}}$ are not considered here), 2) that C_ϵ does not depend strongly on ϵ, which we return to below.

*We note that a linear-dependence of T_c with pressure may also arise from a mutual cancelation between quadratic terms of the two independent A_{1g} components $\frac{1}{2}(\epsilon_{xx}+\epsilon_{yy})$ and ϵ_{zz}, while this requires an unlikely degree of fine-tuning. As a second note, T_c only puts constraints on the free energy close to phase transitions; we hypothesize that when T_c is not strongly modified by ϵ and $\epsilon^2_{A_{1g}}$ terms are excluded near the phase transition, the presence of such terms in the free energy away from T_c is also unlikely.

Elastocaloric Effect in $D_yB_2C_2$: Symmetric and Antisymmetric Strain-Tuning of the Antiferroquadrupolar (AFQ) Phase Transition

Having outlined the symmetry properties of the elastocaloric effect, we apply the above framework to investigate the strain response of a tetragonal rare earth intermetallic DyB_2C_2. DyB_2C_2 crystallizes in the space group $P4/mbm$; as shown in Fig. 2*A*, the Dy square lattice layers are spaced by planar networks of B-C octagon and parallelogram motifs. In Fig. 2*B*, we show an optical image of the experimental setup, where a piece of DyB_2C_2 single crystal shaped into a long, thin plate is mounted on a strain cell and the stress thus experienced by the sample is uniaxial along the in-plane [100] axis (which we denote as x). The temperature oscillation generated by the AC strain via the elastocaloric effect is measured using the thermometer/thermocouple attached to the surface of the sample, and the AC strain frequency is selected such that the system approaches a quasi-adiabatic condition (*Materials and Methods* and *SI Appendix*). In this experiment, we control and measure ϵ_{xx}, while ϵ_{zz} and ϵ_{yy} are left unconstrained; based on Poisson ratios $\nu_{12} = -d\epsilon_{yy}/d\epsilon_{xx} = 0.45$ and $\nu_{13} = -d\epsilon_{zz}/d\epsilon_{xx} = 0.08$ estimated from the elastic moduli tensor of LuB_2C_2 (32) (*Materials and Methods* and *SI Appendix*), we linearly decompose the induced deformation into its components in symmetric and antisymmetric channels with their relative strength as $\frac{1}{2}(\epsilon_{xx}-\epsilon_{yy}) : \frac{1}{2}(\epsilon_{xx}+\epsilon_{yy}) : \epsilon_{zz} = 0.72 : 0.28 : -0.08$ (these numbers are normalized with respect to ϵ_{xx}). The decomposition is schematically illustrated in Fig. 2*C*: The experimentally generated deformation is shown as a green cuboid and its symmetric A_{1g} (antisymmetric B_{1g}) component as blue (red) cuboids. We report the measured elastocaloric coefficient as the oscillation amplitude of T normalized by that of ϵ_{xx} which we experimentally control (therefore the measured quantity can be expressed as $\left.\frac{dT}{d\epsilon_{xx}}\right|^{\sigma_{ij}=0 \text{ except } \sigma_{xx}}_{S=\text{const.}}$); hereafter we denote this as $dT/d\epsilon_{xx}$ unless otherwise stated. We note that $dT/d\epsilon_{xx}$ thus defined contains both $\epsilon_{A_{1g}}$- and $\epsilon_{B_{1g}}$-components (*Materials and Methods*).

The Dy sites in DyB_2C_2 possess a tetragonal local symmetry and the crystal field ground state of Dy^{3+} ($4f^9$) is a quasi-quartet $J_z \approx |\pm\frac{1}{2}\rangle, |\pm\frac{3}{2}\rangle$ within the $J = \frac{15}{2}$ manifold (33). Here J is the total angular momentum operator. This f-electron quartet provides a basis for a two-step phase transition to fully release the $R\ln 4$ entropy (R is the gas constant) and an avenue to order in a time-reversal-symmetric quadrupolar channel (order parameter characterized by $O_{x^2-y^2} \equiv J_x^2 - J_y^2$ and $O_{xy} \equiv J_xJ_y + J_yJ_x$) prior to magnetic order (order parameter characterized by J_x, J_y, J_z). In the quadrupolar order that sets in at about 25 K, the charge distribution of the f electrons breaks the high-temperature local fourfold rotational symmetry and the resulting quadrupole moments (linear superposition of $O_{x^2-y^2}$ and O_{xy}) in neighboring layers are orthogonal to each

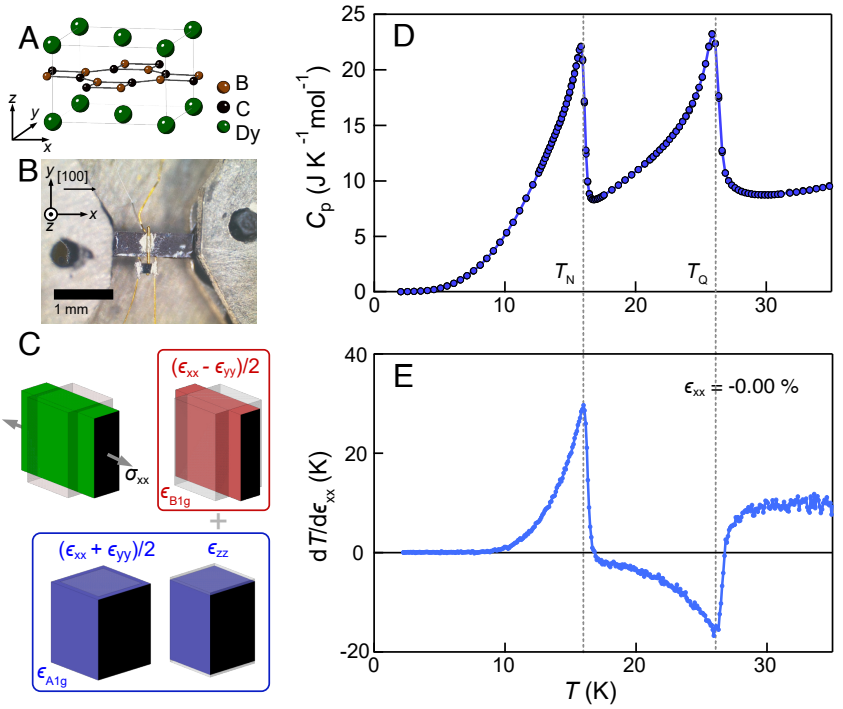

Fig. 2. Elastocaloric effect, quadrupolar and magnetic orders in DyB_2C_2. (*A*) Crystal structure of DyB_2C_2 where Dy atoms are shown in green, B atoms in brown and C atoms in black. The bonds between B and C atoms are also depicted. (*B*) Optical image of a piece of DyB_2C_2 single crystal mounted on a strain cell (see text). The scale bar stands for 1 mm. (*C*) Decomposition of the experimentally generated deformation (green cuboid) into symmetric $\epsilon_{A_{1g}}$ (blue cuboid) and antisymmetric $\epsilon_{B_{1g}}$ (red cuboid) strain channels. The gray box indicates the undeformed tetragonal structure. (*D* and *E*) Heat capacity C_p (*D*) and $dT/d\epsilon_{xx}$ measured without bias strain (*E*) of DyB_2C_2. The location of T_Q and T_N are indicated by gray dashed lines in (*D*) and (*E*).

other, forming an antiferroquadrupole (AFQ) state (19, 34). In this AFQ state, a combined C_4 and translational symmetry (translation operation performed along c) is preserved, analogous to the combined time-reversal and translational symmetry of a Néel order. At 16 K an additional phase transition into a noncollinear canted antiferromagnetic (CAFM) phase takes place; there magnetic moments develop within the *ab*-plane and approximately perpendicular to the charge clouds, resulting in a net magnetization along the {100} axes (19, 35). The two-phase transitions can be traced in the heat capacity C_p (measured using a relaxation method) in Fig. 2*D* (36). We define the higher and lower T anomalies as T_Q (AFQ) and T_N (CAFM), respectively; both phase transitions have been reported to be of second-order nature (19).

In Fig. 2*E*, we show $dT/d\epsilon_{xx}$ taken at nominally zero bias strain $\epsilon_{xx} = 0$. We observe two anomalies with opposite signs in the T-dependence of $dT/d\epsilon_{xx}$, corresponding to T_Q and T_N in C_p in Fig. 2*D*. The qualitative resemblance of the singularities in $dT/d\epsilon_{xx}$ and C_p is related to the fact that both C_p and $dT/d\epsilon_{xx}$ are second-order derivatives of thermodynamic potentials. In analogy to the Ehrenfest relation in thermal expansion at second-order phase transitions (37), we derive a modified Ehrenfest relation for $dT/d\epsilon_{xx}$ (see *SI Appendix A*):

$$\frac{dT_C}{d\epsilon_{xx}} = \frac{\Delta[C(dT/d\epsilon_{xx})]}{\Delta C}, \qquad [4]$$

where the evolution of critical temperature T_C with strain $dT_C/d\epsilon_{xx}$ is related to the jump of $C(dT/d\epsilon_{xx})$ along with that in the heat capacity C at the phase transition. From $dT/d\epsilon_{xx}$ shown in Fig. 2*E* and assuming C_p in Fig. 2*D* provides a reasonable approximation for C in Eq. **4** given the small compressibility of solids, we estimate $dT_N/d\epsilon_{xx} = 45$ K and $dT_Q/d\epsilon_{xx} = -35$ K near $\epsilon_{xx} = 0$.

Having demonstrated that $dT/d\epsilon_{xx}$ can be used to trace both AFQ and CAFM phase transitions in DyB_2C_2, we proceed to the evolution of $dT/d\epsilon_{xx}$ under bias ϵ_{xx}. We first focus on the higher T AFQ phase transition and show the T-dependence of $dT/d\epsilon_{xx}$ between 20 K and 30 K at selected ϵ_{xx} in Fig. 3*A*. A nonzero ϵ_{xx} introduces a number of changes, which we outline as follows. First, the location of T_Q (marked by arrows in Fig. 3*A*) moves with ϵ_{xx}, and the trend is summarized in Fig. 3*B*. Second, at T_Q, a deep, negative jump at the most tensile ϵ_{xx} gradually evolves into a positive, step-like feature at the most compressive ϵ_{xx}. We note that there are intermediate ϵ_{xx} values (between -0.15% and -0.21%) where the singularity associated with T_Q appears vanishingly small; the ϵ_{xx}-evolution of the jump at T_Q of $dT/d\epsilon_{xx}$ (*i.e.* $\Delta(dT/d\epsilon_{xx})$, estimated as $dT/d\epsilon_{xx}(T = T_Q) - dT/d\epsilon_{xx}(30\,\mathrm{K})$) is summarized in Fig. 3*C*. Finally, away from the phase transitions both above and below T_Q, we observe a continuous variation of $dT/d\epsilon_{xx}$ with ϵ_{xx}; we return to these behaviors in section 4.

Eq. **4** suggests that given $dT/d\epsilon_{xx}$ traces at various bias ϵ_{xx}, two independent means exist to trace the strain-dependence of a phase transition: either focusing on the singularity in $dT/d\epsilon_{xx}$ marking T_Q, or the size of jump in $dT/d\epsilon_{xx}$ in conjunction with C at T_Q. The former and latter views of the AFQ phase transition are contrasted in Fig. 3 *B* and *Inset* of *C*, respectively. In the latter, we assume that C for both the ordered and disordered phases near T_Q are independent of ϵ. In Fig. 3*B*, T_Q appears to evolve with ϵ_{xx} both in a linear ϵ_{xx} and quadratic ϵ_{xx}^2 manner. Alternatively, $\Delta[C(dT/d\epsilon_{xx})]/\Delta C$ shown in Fig. 3 *C*, *Inset* appears linear with ϵ_{xx} over the entire ϵ_{xx} range, and a linear

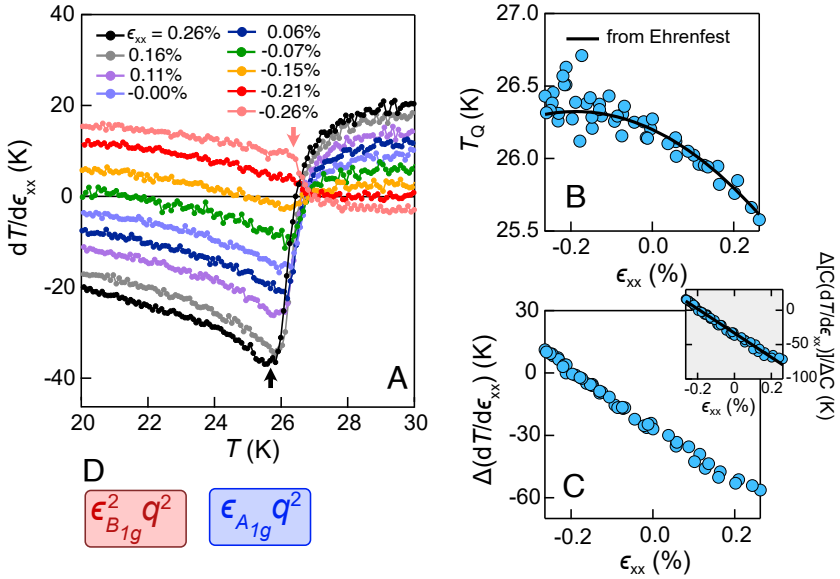

Fig. 3. Strain tuning of the antiferroquadrupolar (AFQ) phase transition in DyB_2C_2. (*A*) T-dependence of $dT/d\epsilon_{xx}$ at selected bias strain ϵ_{xx}. At $\epsilon_{xx} = \pm 0.26\%$, we highlight the discontinuities at T_Q with arrows. (*B* and *C*) Evolution of T_Q (*B*) and $dT/d\epsilon_{xx}$ jump $\Delta(dT/d\epsilon_{xx}) \equiv dT/d\epsilon_{xx}(T = T_Q) - dT/d\epsilon_{xx}(30\,\mathrm{K})$ (*C*) with ϵ_{xx}. *Inset* of (*C*) shows $\Delta[C(dT/d\epsilon_{xx})]/\Delta C$ at T_Q. The solid curve in (*B*) is inferred from the linear fit shown as a black solid line in (*C*) *Inset* (see text). (*D*) Leading coupling between $\epsilon_{A_{1g}}$ ($\epsilon_{B_{1g}}$) and the staggered quadrupolar order parameter q in the free energy enclosed in a blue (red) box.

fit $A + B\epsilon_{xx}$ yields $A = -47.1(7), B = -2.49(4) \times 10^4$. Following Eq. **4**, $\Delta[C(dT/d\epsilon_{xx})]/\Delta C$ should reflect the ϵ_{xx}-evolution of $dT_Q/d\epsilon_{xx}$: in Fig. 3*B* we compare an integration of $A + B\epsilon_{xx}$ multiplied by a factor to account for the imperfect adiabaticity in our experiments (black solid curve) with the directly traced $T_Q(\epsilon_{xx})$ (blue symbols).[†] That the integrated curve agrees with the bare ϵ_{xx}-dependence of T_Q provides an experimental demonstration of the validity of the modified Ehrenfest relation Eq. **4** and additionally suggests that our assumption that the heat capacity is not strongly affected by ϵ is valid. We note that a direct polynomial fit to $T_Q(\epsilon_{xx})$ yields uncertainties of the $\epsilon_{xx}(\epsilon^2_{xx})$-coefficients to be 6% (27%); thanks to its strain-derivative nature, the elastocaloric coefficient at T_Q provides with significantly improved accuracy (1–2% for both ϵ_{xx} and ϵ^2_{xx} terms) a view of the evolution of T_Q with strain.

Following the symmetry-decomposition framework we laid out in Section , we assign the ϵ_{xx} and ϵ^2_{xx} terms in T_Q to the symmetric ($\epsilon_{A_{1g}}$) and antisymmetric ($\epsilon_{B_{1g}}$) strain channels, respectively. They are expected to result from leading terms in the free energy of the form $\epsilon_{A_{1g}} q^2$ ($\epsilon^2_{B_{1g}} q^2$) for $\epsilon_{A_{1g}}$ ($\epsilon_{B_{1g}}$), as shown in Fig. 3*D* (q represents the staggered quadrupolar order parameter). The absence of an $\epsilon^2_{A_{1g}}$ term in T_Q is corroborated by the linear pressure-evolution of T_Q up to hydrostatic pressure of 8 GPa, where the in-plane $\epsilon_{A_{1g}}$ component $\frac{1}{2}(\epsilon_{xx} + \epsilon_{yy})$ reaches -0.8% (14, 31). The above symmetry decomposition allows us to conclude that antisymmetric strain suppresses T_Q in a quadratic manner and that at the highest strain in our experiments (both compressive and tensile), the antisymmetric strain contribution (ϵ^2_{xx} term) becomes comparable and exceeds the symmetric strain contribution (ϵ_{xx} term).

[†]The black solid curve is scaled along the temperature axis by a factor of 4, which we hypothesize originates from an imperfect adiabaticity of our experiments.

Tetragonal-Symmetry-Breaking in the Canted Antiferromagnetic (CAFM) Phase

Having identified considerable contributions from both $\epsilon_{A_{1g}}$ and $\epsilon_{B_{1g}}$ in the strain-modulation of T_Q, we turn to the lower CAFM phase transition. In Fig. 4*A*, starting from ϵ_{xx} on the tensile side $\epsilon_{xx} = 0.26\%$ (black curve), the peak in $dT/d\epsilon_{xx}$ at T_N sits on top of a continuously varying background, and its height is initially not much varied by decreasing ϵ_{xx}; below $\epsilon_{xx} = -0.1\%$, however, a downward peak resembling a horizontal mirror image of the peak at $\epsilon_{xx} > 0$ abruptly emerges. This can be contrasted with the continuous variation of the phase transition jumps at T_Q in Fig. 3*A*. In Fig. 4 *B* and *C*, we trace the location of these peaks in $dT/d\epsilon_{xx}$ and the height of the associated jumps $\Delta(dT/d\epsilon_{xx})$, respectively. Due to the presence of multiple singular features at $\epsilon_{xx} = -0.2 \sim -0.13\%$, in Fig. 4 *B* and *C* we mark the peaks with the respective symbol sizes proportional to their peak widths (*SI Appendix*).

In Fig. 4*B*, we can identify a "V-shape" in the $T - \epsilon_{xx}$ plane with its two branches marked by the primary positive and negative peak features, respectively; this is accompanied by a step-wise structure of $\Delta(dT/d\epsilon_{xx})$ as a function of ϵ_{xx} displayed in Fig. 4*C*. The "branched" phase boundary structure prompts us to propose the emergence of two distinct sets of domains below T_N that are strain-selective. Above $\epsilon_{xx} = -0.13\%$, a linear fit to $\Delta[C(dT/d\epsilon_{xx})]/\Delta C$ (Fig. 4 *C*, *Inset*) yields $A = 66.6(8), B = -3(6) \times 10^2$ ($A + B\epsilon_{xx}$), which via Eq. **4** suggests a linear dependence of T_N with ϵ_{xx}, consistent with our observation (Fig. 4*B*[‡]; we note that the B coefficient, which via Eq. **4** is associated with a potential ϵ^2_{xx} term in $T_N(\epsilon_{xx})$, cannot be distinguished from zero and is at least two orders of magnitude smaller than its counterpart in $T_Q(\epsilon_{xx})$.

[‡]To quantitatively compare $A\epsilon_{xx}$ with $T_N(\epsilon_{xx})$ in Fig. 4*B*, an additional factor 2.3 is required in front of *A*. We note that this factor introduced to account for imperfect adiabaticity is comparable with that used above for T_Q. The difference between the two factors may arise from a T-dependence of the thermal conditions (thus the adiabaticity) of the experimental setup.

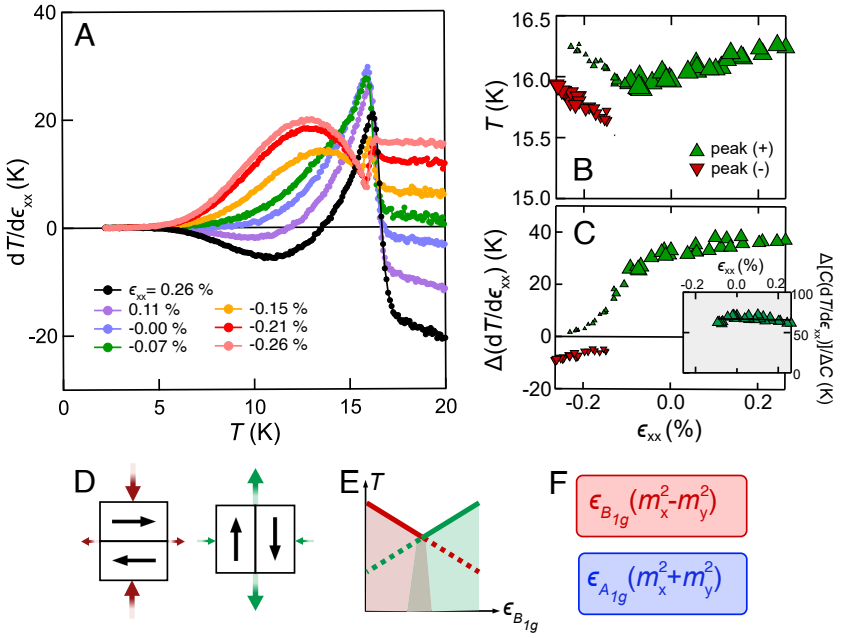

Fig. 4. Strain tuning of the canted antiferromagnetic (CAFM) phase transition in DyB_2C_2. (*A*) $dT/d\epsilon_{xx}$ at selected ϵ_{xx} below 20 K. (*B*) $T-\epsilon_{xx}$ phase diagram for the CAFM phase. Green and red triangle symbols are extracted from locations of positive and negative peaks in $dT/d\epsilon_{xx}(T)$, respectively. (*C*) $\Delta(dT/d\epsilon_{xx})$ as a function of ϵ_{xx}. The size of the symbols in (*B*) and (*C*) is proportional to natural logarithm of the peak width determined from zeros of the *T*-derivative of $dT/d\epsilon_{xx}$. *Inset* of (*C*) shows $\Delta[C(dT/d\epsilon_{xx})]/\Delta C$ of the positive peaks and the solid black line depicts a linear fit. (*D*) Schematic of the two sets of the fourfold CAFM domains; black arrows indicate the orientation of net magnetization *m*, and thick colored arrows illustrate the strain that selects these domains. (*E*) Tuning of T_N of the two domains with $\epsilon_{B_{1g}}$. The solid (dashed) lines indicate T_N of the favored (unfavored) domain. (*F*) Coupling terms between $\epsilon_{B_{1g}}$ and $\epsilon_{A_{1g}}$ to the CAFM net moment *m* to the leading order: $\epsilon_{B_{1g}}(m_x^2-m_y^2)$ (red box) and $\epsilon_{A_{1g}}(m_x^2+m_y^2)$ (blue box).

Below, we discuss the nature of the strain-selective domains and the linear evolution of T_N with ϵ. In the CAFM phase of DyB_2C_2, it is known that there exists net magnetization *m* along in-plane {100} directions (19, 35); via magnetoelastic coupling (38), these domains can distort along {100} below T_N, providing a natural origin for the proposed strain-selective domains. The lowest order magnetoelastic coupling is required to take the form of ϵm^2 to be invariant under time-reversal symmetry (38), and we group the four {100} magnetic domains into subgroups with *m* along $\pm x$ and $\pm y$, as illustrated in Fig. 4*D*. Additionally taking into account C_4 (for discussions hereafter, we still adopt the convention of the high *T* D_{4h} group), we may decompose ϵm^2 into terms containing antisymmetric $\epsilon_{B_{1g}}(m_x^2-m_y^2)$ and symmetric strain $\epsilon_{A_{1g}}(m_x^2+m_y^2)$, respectively (39). We note that the consequences of the $\epsilon_{B_{1g}}$ term are twofold: It selects among the differently distorted domains, and promotes the order within the favored domains while suppressing that of the other type (both in an ϵ-linear fashion), as we illustrate in Fig. 4*E*; joining $T_N(\epsilon_{B_{1g}})$ of the favored domains yields a V-shape, akin to that observed in Fig. 4*B*. We note that similar phase diagrams have been discussed for antisymmetric strain manipulation of in-plane charge density wave orders in tetragonal $(Er,Tm)Te_3$ (10) and in the context of $p_x \pm ip_y$-type multicomponent superconducting phases (3), both with similar forms of order parameter-antisymmetric strain coupling. We note that the deviation of the center of the "V-shape" in Fig. 4*B* from zero bias strain (nominally defined as the state the system is cooled down to with zero bias voltage on the piezoelectric stacks) may result from a differential thermal contraction between the strain cell and the sample.

In Fig. 5*A*, we show $dT/d\epsilon_{xx}$ taken in strain scans at selected *T*: above T_N $dT/d\epsilon_{xx}$ appears linear in ϵ over the measured strain range, while below T_N a nonlinear component develops; below 12 K a strain-hysteresis additionally opens up. Both nonlinearity and hysteresis in $dT/d\epsilon_{xx}(\epsilon_{xx})$ are consistent with ϵ-selectivity of the CAFM domains: We attribute the positive strain limit where the system reaches a constant slope to a state with a single type of orientational domains, which is separated by a multidomain state from a state with the alternative set of orientational domains (see *Insets* of Fig. 5 *A*). The domain selection necessarily arises from antisymmetric strain and requires an $\epsilon_{B_{1g}}$ lattice distortion in each of the domains, and is also consistent with strain (or more precisely, one component of the strain tensor), instead of stress, being the thermodynamic quantity that is held constant in our experiments (40).

The symmetry-lowering at the CAFM phase is additionally evidenced by the mapping of thermally modulated optical birefringence shown in Fig. 4 *B–D*; a similar technique had been used to image nematic domains in other systems (41) (Additional information on the optical setup can be found in *SI Appendix*). In Fig. 4*B*, two types of domains with their principal axes near the crystallographic {100} orientations (Fig. 4 *C* and *D*) can be identified, and their domain wall appears to run approximately 45° between the principal axes. The birefringence imaging confirms the broken C_4 with an orthorhombicity developing along {100} below T_N, and complements the above thermodynamic evidence of tetragonal symmetry-breaking in the CAFM phase. The observed diagonal domain wall is also consistent with that commonly observed on surfaces of ferromagnets with fourfold easy axes in the plane (42). It has been suggested previously that magnetic order in DyB_2C_2 is accompanied by slight rotation of quadrupole moments from a staggered arrangement due to a competition between quadrupolar exchange and magnetic exchange interactions, and as a result, the crystalline symmetry is lowered from tetragonal to orthorhombic (35); that

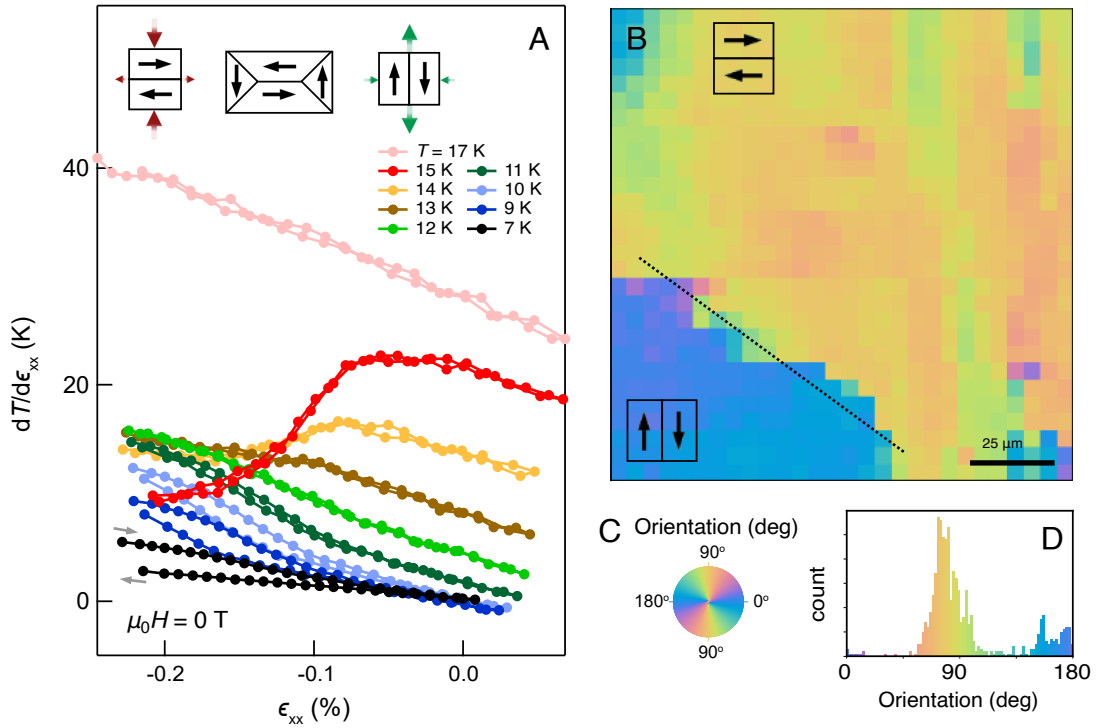

Fig. 5. Tetragonal symmetry-breaking in the CAFM phase of DyB_2C_2. (*A*) ϵ_{xx}-hysteresis of $dT/d\epsilon_{xx}$ at selected T at zero magnetic field. The schematics at the top illustrate the favored domains on the compressive (*Left*) and tensile (*Right*) strain side, respectively. The pink curve ($T = 17$ K) is offset by 30 K for clarity. The gray arrows indicate the direction of the ϵ_{xx}-scans in the hysteresis. (*B*) Map of principal axis orientation over a $130 \times 130\,\mu m^2$ area with a step size of 5 μm with the orientation defined in (*C*). The dashed line is a guide to the eye outlining an observed domain boundary. (*D*) Histogram of orientations shown in (*B*), indicating two domains whose optic axes are offset by 90° from one another. Measurements in (*B–D*) were taken at 2.5 K.

the CAFM phase is potentially monoclinic is proposed in a thermal expansion study (43). Our experimental observations at present cannot rule out a monoclinic nature of the CAFM phase, while we can set a bound that the highest point group symmetry of the CAFM phase is orthorhombic with the in-plane principal axes along the high-temperature tetragonal {100} orientations.

Antisymmetric Elastocaloric Effect from Staggered Quadrupole Moments

In the preceding sections, we focused on the strain tuning of T_Q and T_N; in the following, we examine the overall strain responses in the system not limited to the proximity of the phase transitions. The intertwined magnetic and quadrupolar degrees of freedom motivate us to use a small polarizing magnetic field to eliminate complications from hysteretic and multidomain behaviors. $dT/d\epsilon_{xx}$ obtained with a magnetic field of 0.3 T parallel to [100] (also the stress direction) are summarized in Fig. 6*A* (see *SI Appendix* for $M(H)$ hysteresis of an unstrained sample). We note that the application of H appears to simplify $dT/d\epsilon_{xx}$ near T_N as compared to the zero field responses (i.e., the peak does not reverse in sign as a function of ϵ_{xx}, in contrast to the zero field cases seen in Fig. 4*A* and *SI Appendix*, Fig. S6) and that the peak at T_N in H is rounded due to the presence of a finite net magnetization. $dT/d\epsilon_{xx}$ at different ϵ_{xx} in Fig. 6*A* appear to be composed of an ϵ_{xx}-independent contribution to $dT/d\epsilon_{xx}$ (which can be approximated by the blue trace at $\epsilon_{xx} = 0.01\%$) and a component that varies monotonically with ϵ_{xx}. In Fig. 6*B*, we examine constant-T ϵ_{xx} cuts of $dT/d\epsilon_{xx}$. The ϵ_{xx}-linear dependence of $dT/d\epsilon_{xx}$ over the entire strain-range at all T in Fig. 6*B* can be contrasted with the nonlinear $dT/d\epsilon_{xx}$ in Fig. 5*A*, and is consistent with a single domain state below T_N in field.

Results of linear fits to ϵ_{xx}-cuts of $dT/d\epsilon_{xx}$ at 0.3 T are summarized in Fig. 6*C*; in Fig. 6*C*, we also include both the intercept and slope extracted from zero field $dT/d\epsilon_{xx}$ above T_N as dark blue circles: The close comparison between 0 T and 0.3 T responses above T_N is consistent with the time-reversal-symmetric nature of the quadrupolar order. That the T-trace of the intercept of $dT/d\epsilon_{xx}$ (Fig. 6 *C*, *Inset*) compares closely to the responses at T_N on the tensile strain side at zero field (Fig. 4*A*) suggests that the magnetic domain favored by H coincides with that favored by tensile ϵ_{xx}, from which we infer that the long axis of the distorted unit cell is along m (Fig. 6 *A*, *Inset*). Hereafter we focus on the ϵ_{xx}-slope of $dT/d\epsilon_{xx}$ (main panel of Fig. 6*C*). As we invoke above, the ϵ-odd component in $dT/d\epsilon$ by symmetry originates from antisymmetric strain (Fig. 1*G*), which in the present case is $\epsilon_{B_{1g}}$: Viewed alongside Eq. **1**, above T_Q, $d^2T/d\epsilon^2 > 0$ indicates a quadratic decrease of S with $\epsilon_{B_{1g}}$, consistent with strain suppression of paraquadrupolar fluctuations; similar ϵ-dependence of S has been reported in iron-based superconductors above the nematic phase transition and attributed to a bilinear coupling between antisymmetric strain and underlying nematic fluctuations (28). Below T_Q, $d^2T/d\epsilon^2 < 0$ implies on the contrary a quadratic increase of S with $\epsilon_{B_{1g}}$. In Fig. 6*D*, we show a contour plot of the entropy landscape with $\epsilon_{B_{1g}}$ inferred from the slope in Fig. 6*C* and the zero strain heat capacity (see *SI Appendix* for the procedure to extract $S(\epsilon, T)$ and thus deduce $C(\epsilon, T)$ (27)) near T_Q, where a curvature change in the entropy landscape across T_Q is apparent.

To shed light on the antisymmetric strain effects on the AFQ order and the underlying staggered quadrupolar arrangement, we

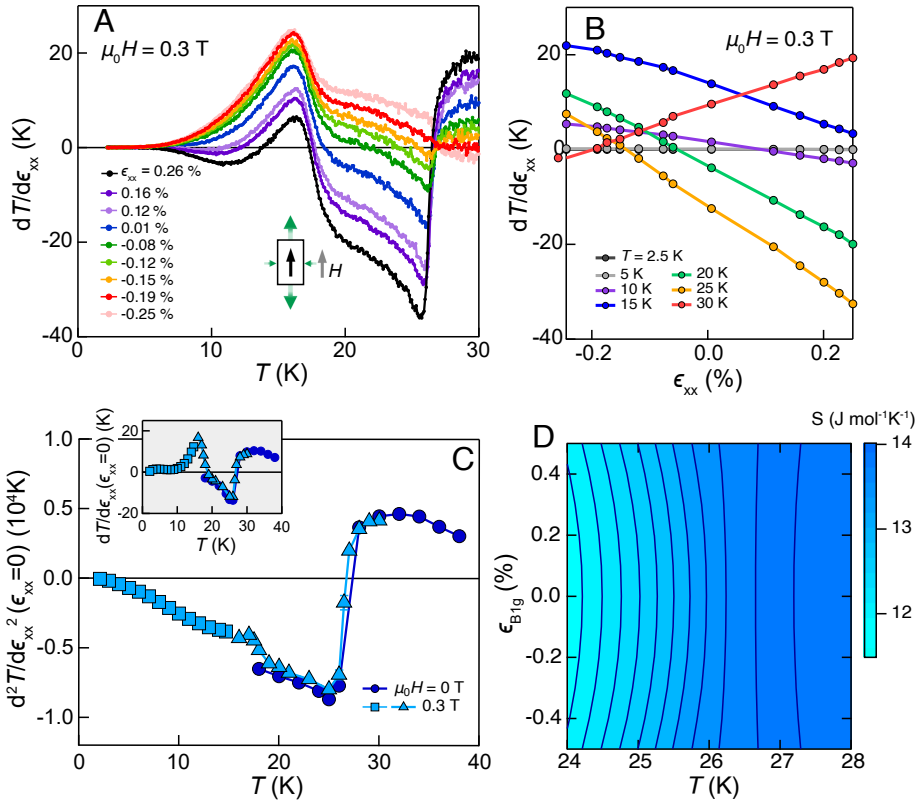

Fig. 6. Antisymmetric elastocaloric effect in DyB_2C_2. (*A*) $dT/d\epsilon_{XX}$ at ϵ_{XX} in an applied magnetic field H along [100] of 0.3 T. *Inset* shows a schematic of the orientation of H, the selected magnetic domain, and an applied tensile strain ($\epsilon_{XX} > 0$). (*B*) Constant T-cuts of $dT/d\epsilon_{XX}$ at selected T. (*C*) ϵ_{XX}-slope of $dT/d\epsilon_{XX}$ as a function of T. *Inset* shows the intercept at $\epsilon_{XX} = 0$. Light (dark) blue symbols are linear fit parameters extracted at 0.3 T (0 T). The triangular and circular symbols are extracted from data taken at a fixed strain frequency of 27.1 Hz while square symbols from data taken at adjusted strain frequencies with T (*SI Appendix*). (*D*) Entropy landscape with respect to $\epsilon_{B_{1g}}$ inferred from (*C*) (*SI Appendix*) near T_Q.

introduce the following Hamiltonian

$$H = K \sum_{<i,j>} O_i O_j - g\epsilon_{B_{1g}} \sum_i O_i \qquad [5]$$

where the first term describes the quadrupole-quadrupole interaction between the nearest neighbors ($K > 0$ gives an AFQ order) and the second term the quadrupole-strain coupling with $g > 0$ (13, 44). Eq. **5** can be further mapped onto an effective AFM Ising model with the quadrupole moments O mapping onto Ising spins S^z and $\epsilon_{B_{1g}}$ mapping onto an effective magnetic field H_z ($J > 0$) (Fig. 7*A*):

$$H = J \sum_{<i,j>} S_i^z S_j^z - H_z \sum_i S_i^z, \qquad [6]$$

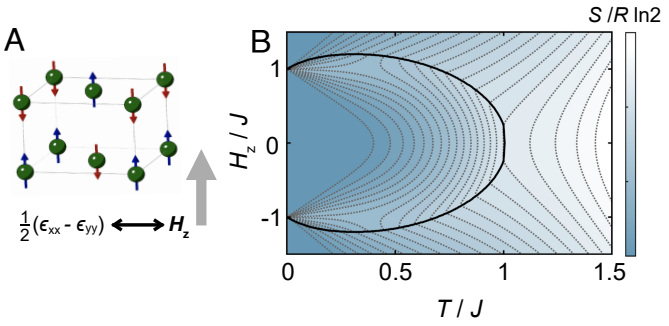

Fig. 7. Antiferromagnetic (AFM) Ising model. (*A*) Schematic of an effective AFM Ising model where an antiferromagnetic spin arrangement corresponds to the antiferroquadrupole order in DyB_2C_2 and the effective magnetic field H_z corresponds to $\epsilon_{B_{1g}}$ (see text). (*B*) Entropy landscape of the AFM Ising model in the $H_z - T$ plane. The black solid curve in (*B*) marks the phase boundary between the AFM and paramagnetic phases. An H_z-independent phonon contribution is also included in order to obtain (*B*).

whose mean-field entropy landscape is shown in Fig. 7*B* (here we also include a field-independent phonon background, see *SI Appendix*). In Fig. 7*B*, H_z appears to suppress the critical temperature of the AFM order (similar to $\epsilon_{B_{1g}}$ for the AFQ order), near which the curvature of the isentropic contours exhibits a sharp change, giving rise to a sign reversal of the antisymmetric slope (*SI Appendix*) similar to that observed experimentally in Fig. 6 *C* and *D*. The comparison suggests that within the ordered state, the antisymmetric strain ($\epsilon_{B_{1g}}$ in this case) destabilizes and therefore suppresses the staggered AFQ order akin to how magnetic field destabilizes a staggered Ising antiferromagnetic order by exciting pseudospin flips (quadrupole flops). The nonmonotonic shape of the phase boundary in the (T, H_z) plane near $T = 0$ has been discussed before for AFM Ising models and attributed to an order-by-disorder effect (45, 46). We note that the effective AFM Ising model has only taken into account the quadrupolar degrees of freedom; the continuity of the observed antisymmetric response above and below T_N aside from a small kink at T_N in Fig. 6*C* implies that the overall staggered quadrupole configuration is likely not fundamentally modified (a weak relative reorientation of the quadrupole moments has been

suggested by ref. 35) by the magnetic order and is the source of the observed ϵ-linear responses in $dT/d\epsilon$.

Discussion and Summary

In summary, we have employed the AC elastocaloric effect to investigate the strain responses of the f-electron antiferroquadrupolar order in DyB_2C_2. The strain-dependence of both the quadrupolar and magnetic phase transitions in the system can be precisely characterized by the jump of the elastocaloric signals—the former contains both linear and quadratic strain-dependences while the latter remain linear over the explored strain range. While symmetric strain $\epsilon_{A_{1g}}$ always appears to tune both T_N and T_Q in a linear manner, the antisymmetric strain $\epsilon_{B_{1g}}$, which is inaccessible in hydrostatic pressure experiments, plays an indispensable and more versatile role in controlling T_Q and T_N: for the AFQ phase, $\epsilon_{B_{1g}}$ suppresses T_Q in a quadratic manner, while for the CAFM order, the primary role of $\epsilon_{B_{1g}}$ is found to be twofold: domain selection as well as linearly tuning T_N. The distinct behavior of the two phase transitions with $\epsilon_{B_{1g}}$ lies in the different forms of coupling between $\epsilon_{B_{1g}}$ and the underlying order parameters $\epsilon^2_{B_{1g}} q^2$ and $\epsilon_{B_{1g}}(m_x^2 - m_y^2)$ (Figs. 3*D* and 4*F*); in this context, we may in turn use the evolution of critical temperatures with antisymmetric strain to place strong constraints on the spatial/lattice symmetry of the underlying order parameters given a generic phase transition.

From a symmetry perspective, f-electron-based quadrupolar orders can be viewed as a close analogue of the nematic phases observed in a number of transition-element-based strongly correlated electron systems (18, 47). The relatively well-localized nature of the electronic degrees of freedom and the strong magnetoelastic coupling of f-electrons marks them as model systems to drive quantum phase transitions with strain. For instance, it has been proposed that antisymmetric strain orthogonal to a globally uniform ferroquadrupolar order couples to the latter as an effective transverse field, therefore promoting quantum fluctuations and ultimately driving a quantum phase transition into the Ising nematic order (20). In the present case of an antiferroquadrupolar order, we demonstrate that the antisymmetric strain suppresses the AFQ phase transition, likely through introducing quadrupole flops (pseudospin flips) as an effective "longitudinal field" in the AFM Ising model (we note that we do not exclude transverse field-like effects akin to those proposed in ref. 20). Extrapolating from the measured $T_Q(\epsilon_{B_{1g}})$, we expect that antisymmetric strain on the order of 3–4% may be required to completely suppress the AFQ order and drive a quantum phase transition in the present system. Our study provides a proof-of-principle example of employing antisymmetric strain as a means of driving quantum phase transitions in spatially varying anisotropic electronic orders beyond a uniform rotation–symmetry–breaking nematic order; as briefly discussed in the introduction, examples of systems to which we can extend the above study include orbital order (21, 22), spin and charge stripe order (23, 24), and "hidden," multipolar orders (25).

Viewed alternatively from the perspective of employing elastocaloric effect as a tool to study strain responses, our results establish that the elastocaloric coefficients provide a refined picture of strain-evolution of given phase transitions, via a modified Ehrenfest relation thanks to its thermodynamic and strain-derivative nature. Additionally, our case study here demonstrates that extending the elastocaloric measurement over a range of strain values provides a pathway to systematically extract effects from spatially symmetric and antisymmetric strains; we anticipate that this framework can be applied as a powerful organizing principle for exploring strain responses of extended classes of quantum materials.

Materials and Methods

Single-Crystal Growth and Characterization. The experiments reported in this paper were performed using high-quality single-crystal samples of DyB_2C_2. Polycrystalline DyB_2C_2 was first prepared by melting together Dy ingots, B pellets and graphite rods in a monoarc furnace. Single crystals of DyB_2C_2 were then grown using the Czochralski method in a tetra arc furnace (GES Corporation, TAC-35325J) in an Ar atmosphere. Typical current used during the growth is 25 A per arc, and single crystalline rods were pulled out from the melt at a rate of approximately 4 mm/h. The obtained rods cleave along (001) planes, and we confirmed the phase and orientation of the obtained crystals using X-ray diffraction. Magnetization measurements were performed in a Quantum Design MPMS-3 SQUID Magnetometer.

Elastocaloric Measurements. Elastocaloric measurements at cryogenic temperatures were performed using a Razorbill CS-100 uniaxial stress cell in a Quantum Design Physical Property Measurement System (PPMS). The crystals were shaped into long rectangular plates and attached to Ti plates using Stycast FT-2850 cured at 80°C for at least 3 h. In main text Fig. 2*B*, we show an optical image of a DyB_2C_2 crystal used in the elastocaloric measurements. The single crystalline piece of DyB_2C_2 is mounted on the strain cell with the uniaxial stress applied along the in-plane [100] direction. The sample dimension was 2.66 mm × 0.43 mm × 0.032 mm, and the effective strained length between the two Ti mounting plate is 1.628 mm. The temperature oscillations were measured using either an Au(0.07%Fe)-chromel thermocouple or a RuO_x thermometer (for clarity, the experimental data shown in the main text are all obtained from the latter); the former is attached to the sample via a thin layer of AngstromBond AB9110LV (Fiber Optic Center) while the latter is thermally connected to the sample via a 50 μm-gold wire. Additional silver paste (Dupont 4929N) is applied onto the gold wire to enhance the thermal coupling between the sample and the thermometer. The thermometer near the sample is connected to three identical thermometers thermally anchored at the bath forming a full Wheatstone bridge to single out the temperature oscillation in response to the applied AC strain. In the experiments, an AC strain with a frequency ω_ϵ is applied through the outer stack of CS-100, and the sine-out output of lock-in amplifier SR860 (Stanford Research Systems) is first amplified with TEGAM-2350 High-Voltage Power Amplifier (by a factor of 50) before reaching the piezoelectric stacks. The inner piezoelectric stack is powered through an auxiliary DC output of SR860 amplified via an SVP 150 bip/1 High-Voltage Amplifier (Piezomechanik) by a factor of 50. Typical AC strain oscillation amplitude used in the experiments is approximately 5×10^{-5}. The temperature (voltage) responses from the thermocouple are captured at the frequency ω_ϵ while that from the thermometer is captured at the frequency $(\omega_\epsilon - \omega_I)$ where ω_I is the AC current excitation applied to the bridge circuit. We used current frequency of 1.4 kHz and AC strain frequency of 27.1 Hz in data shown in Figs. 2–5 and 6 *A* and *B* while the low temperature ($T < 12$ K) slope in Fig. 6*C* are extracted from measurements taken with AC strain frequencies adjusted for each temperature to account for the shifting optimal frequency windows (*SI Appendix*).

Mechanical State in the Elastocaloric Experiments. In our experiments, the longitudinal strain ϵ_{xx} is the thermodynamic control parameter, and the sample is under such a mechanical state that the only finite component in the stress tensor σ_{ij} is σ_{xx}. The measured elastocaloric coefficient is denoted as $(dT/d\epsilon_{xx})$ for simplicity while we note that it is a linear combination of the following partial derivatives multiplied by the respective Poisson ratios:

$$\frac{dT}{d\epsilon_{xx}} = \left(\frac{\partial T}{\partial \epsilon_{xx}}\right)_S + \left(\frac{\partial T}{\partial \epsilon_{yy}}\right)_S \frac{d\epsilon_{yy}}{d\epsilon_{xx}} + \left(\frac{\partial T}{\partial \epsilon_{zz}}\right)_S \frac{d\epsilon_{zz}}{d\epsilon_{xx}}. \quad [7]$$

The Poisson ratios between $\epsilon_{xx,yy,zz}$ under our experimental condition can be solved from the following set of linear equations through the elastic moduli tensor of LuB_2C_2 (32):

$$\begin{pmatrix}\sigma_{xx}\\0\\0\end{pmatrix}=\begin{pmatrix}525&243&34\\243&525&34\\34&34&224\end{pmatrix}[\mathrm{GPa}]\times\begin{pmatrix}\epsilon_{xx}\\\epsilon_{yy}\\\epsilon_{zz}\end{pmatrix}, \quad [8]$$

from $\sigma_{yy}=\sigma_{zz}=0$ we obtain $\nu_{13}=-\epsilon_{zz}/\epsilon_{xx}=0.08$, $\nu_{12}=-\epsilon_{yy}/\epsilon_{xx}=0.45$.

Eq. **7** can be alternatively expressed in its symmetric and antisymmetric components (here $\epsilon_{x^2+y^2}=\frac{1}{2}(\epsilon_{xx}+\epsilon_{yy})$ and $\epsilon_{x^2-y^2}=\frac{1}{2}(\epsilon_{xx}-\epsilon_{yy})$):

$$\frac{dT}{d\epsilon_{xx}}=\left(\frac{\partial T}{\partial\epsilon_{x^2+y^2}}\right)_S\frac{d\epsilon_{x^2+y^2}}{d\epsilon_{xx}}+\left(\frac{\partial T}{\partial\epsilon_{zz}}\right)_S\frac{d\epsilon_{zz}}{d\epsilon_{xx}}+\left(\frac{\partial T}{\partial\epsilon_{x^2-y^2}}\right)_S\frac{d\epsilon_{x^2-y^2}}{d\epsilon_{xx}}, \quad [9]$$

where $d\epsilon_{x^2+y^2}/d\epsilon_{xx}=\frac{1-\nu_{12}}{2}$ and $d\epsilon_{x^2-y^2}/d\epsilon_{xx}=\frac{1+\nu_{12}}{2}$. The first (second) row of Eq. **9** denotes the symmetric ϵ_{A1g} (antisymmetric ϵ_{B1g}) responses.

ϵ–T Ehrenfest Relation. Here, we consider in the ϵ–T plane two phases 1 and 2 that are separated from each other by a second-order phase transition with critical temperature $T_C(\epsilon)$. The state variables of the two phases, such as entropy $S_{1,2}$, should be continuous everywhere along the phase boundary $T_C(\epsilon)$ in the $\epsilon-T$ plane ($S_1=S_2|_{T_C}$). Taking an infinitesimal variation of both S_1 and S_2 along $T_C(\epsilon)$ results in $dS_1=dS_2|_{T_C}$, which requires

$$\left(\frac{\partial S_1}{\partial T}\right)_\epsilon dT+\left(\frac{\partial S_1}{\partial\epsilon}\right)_T d\epsilon=\left(\frac{\partial S_2}{\partial T}\right)_\epsilon dT+\left(\frac{\partial S_2}{\partial\epsilon}\right)_T d\epsilon, \quad [10]$$

along $T_C(\epsilon)$. This suggests that

$$\frac{dT_C}{d\epsilon}=\frac{(\partial S_1/\partial\epsilon)_T-(\partial S_2/\partial\epsilon)_T}{(\partial S_2/\partial T)_\epsilon-(\partial S_1/\partial T)_\epsilon}. \quad [11]$$

Using $TdS=C_\epsilon dT$ and Eq. **1** we get

$$\frac{dT_C}{d\epsilon}=\frac{C_1(\partial T_1/\partial\epsilon)_S-C_2(\partial T_2/\partial\epsilon)_S}{C_1-C_2}, \quad [12]$$

where C_1 and C_2 are the heat capacity of the two phases at T_C. Eq. **12** may be reformulated as

$$\frac{dT_C}{d\epsilon}=\frac{\Delta[C(\partial T/\partial\epsilon)_S]}{\Delta C}, \quad [13]$$

analogous to the Ehrenfest relation relating the phase boundary with respect to uniaxial pressure $T_C(P_i)$ to the jumps at thermal expansion α_i and heat capacity (37):

$$\frac{dT_C}{dP_i}=V_mT_C\frac{\Delta\alpha_i}{\Delta C}, \quad [14]$$

Here V_m is the molar volume.

The above derivation is based on a generic form of applied ϵ. Taking into account the experimentally relevant linear combination of strain modes discussed in the main text, the modified Ehrenfest relation in the context of our experiments can be expressed as

$$\left.\frac{dT_C}{d\epsilon_{xx}}\right|_{\boldsymbol{\sigma}=\sigma_{xx}}=\frac{\Delta[C(dT/d\epsilon_{xx})|_{\boldsymbol{\sigma}=\sigma_{xx}}]}{\Delta C}, \quad [15]$$

where $(dT/d\epsilon_{xx})|_{\boldsymbol{\sigma}=\sigma_{xx}}$ is the experimentally measured elastocaloric coefficient.

Data, Materials, and Software Availability. Spreedsheet data have been deposited in Stanford Digital Repository (https://doi.org/10.25740/wy533np2837) (36).

ACKNOWLEDGMENTS. We thank R.M. Fernandes and A.P. Mackenzie for fruitful discussions. Experimental work performed at Stanford University was funded by the Gordon and Betty Moore Foundation EPiQS Initiative, grant GBMF9068. L.Y. also acknowledges support by the Marvin Chodorow Postdoctoral Fellowship at the Department of Applied Physics, Stanford University. M.D.B. acknowledges support by the Geballe Laboratory for Advanced Materials Fellowship. Optical measurements were performed at the Lawrence Berkeley Laboratory as part of the Quantum Materials program, Director, Office of Science, Office of Basic Energy Sciences, Materials Sciences and Engineering Division, of the US Department of Energy under Contract No. DE-AC02-05CH11231. V.S. is supported by the Miller Institute for Basic Research in Science, UC Berkeley. J.O. and Y.S. received support from the Gordon and Betty Moore Foundation's EPiQS Initiative through Grant GBMF4537 to J.O. at UC Berkeley. J.F.R.-N. acknowledges support from the Gordon and Betty Moore Foundation's EPiQS Initiative through Grants GBMF4302 and GBMF8686.

Author affiliations: [a]Geballe Laboratory for Advanced Materials, Stanford University, Stanford, CA 94305; [b]Department of Applied Physics, Stanford University, Stanford, CA 94305; [c]Department of Physics, University of California, Berkeley, CA 94720; [d]Materials Science Division, Lawrence Berkeley National Laboratory, Berkeley, CA 94720; and [e]Department of Physics, Stanford University, Stanford, CA 94305

Author contributions: L.Y. and I.R.F. designed research; L.Y., Y.S., V.S., M.S.I., T.W., and M.D.B. performed research; L.Y., J.F.R.-N. and M.E.S. contributed new reagents/analytic tools; L.Y., Y.S., V.S., and J.O. analyzed data; and L.Y. and I.R.F. wrote the paper.

1. J. Olsen *et al.*, Superconductivity under pressure. *Rev. Mod. Phys.* **36**, 168 (1964).
2. C. W. Hicks, M. E. Barber, S. D. Edkins, D. O. Brodsky, A. P. Mackenzie, Piezoelectric-based apparatus for strain tuning. *Rev. Sci. Inst.* **85**, 065003 (2014).
3. C. W. Hicks *et al.*, Strong increase of T_c of Sr_2RuO_4 under both tensile and compressive strain. *Science* **344**, 283–285 (2014).
4. A. Steppke *et al.*, Strong peak in T_c of Sr_2RuO_4 under uniaxial pressure. *Science* **355**, eaaf9398 (2017).
5. E. Dagotto, Complexity in strongly correlated electronic systems. *Science* **309**, 257–262 (2005).
6. P. Malinowski *et al.*, Suppression of superconductivity by anisotropic strain near a nematic quantum critical point. *Nat. Phys.* **16**, 1189–1193 (2020).
7. I. Kostylev, S. Yonezawa, Z. Wang, Y. Ando, Y. Maeno, Uniaxial-strain control of nematic superconductivity in $Sr_xBi_2Se_3$. *Nat. Commun.* **11**, 1–8 (2020).
8. T. Worasaran *et al.*, Nematic quantum criticality in an Fe-based superconductor revealed by strain-tuning. *Science* **372**, 973–977 (2021).
9. H. H. Kim *et al.*, Uniaxial pressure control of competing orders in a high-temperature superconductor. *Science* **362**, 1040–1044 (2018).
10. J. Straquadine, M. Ikeda, I. Fisher, Evidence for realignment of the charge density wave state in $ErTe_3$ and $TmTe_3$ under uniaxial stress via elastocaloric and elastoresistivity measurements. *Phys. Rev. X* **12**, 021046 (2022).
11. M. E. Barber *et al.*, Suppression of superconductivity by charge density wave order in $YBa_2Cu_3O_{6.67}$. arXiv [Preprint] (2021). https://doi.org/10.48550/arXiv.2101.02923 (Accessed 1 December 2021).
12. J. F. Nye, *Physical Properties of Crystals: Their Representation by Tensors and Matrices* (Oxford University Press, 1985).
13. B. Lüthi, *Physical Acoustics in the Solid State* (Springer Science & Business Media, 2007), vol. 148.
14. M. S. Ikeda *et al.*, Symmetric and antisymmetric strain as continuous tuning parameters for electronic nematic order. *Phys. Rev. B* **98**, 245133 (2018).
15. M. Shapiro, P. Hlobil, A. Hristov, A. V. Maharaj, I. Fisher, Symmetry constraints on the elastoresistivity tensor. *Phys. Rev. B* **92**, 235147 (2015).
16. P. Wiecki *et al.*, Dominant in-plane symmetric elastoresistance in $CsFe_2As_2$. *Phys. Rev. Lett.* **125**, 187001 (2020).
17. L. Wang *et al.*, Electronic nematicity in URu_2Si_2 revisited. *Phys. Rev. Lett.* **124**, 257601 (2020).
18. E. W. Rosenberg, J. H. Chu, J. P. Ruff, A. T. Hristov, I. R. Fisher, Divergence of the quadrupole-strain susceptibility of the electronic nematic system $YbRu_2Ge_2$. *Proc. Natl. Acad. Sci. U.S.A.* **116**, 7232–7237 (2019).
19. H. Yamauchi *et al.*, Antiferroquadrupolar ordering and magnetic properties of the tetragonal DyB_2C_2 compound. *J. Phys. Soc. Jpn.* **68**, 2057–2066 (1999).
20. A. V. Maharaj *et al.*, Transverse fields to tune an Ising-nematic quantum phase transition. *Proc. Natl. Acad. Sci. U.S.A.* **114**, 13430–13434 (2017).
21. K. I. Kugel, D. Khomskiĭ, The Jahn–Teller effect and magnetism: Transition metal compounds. *Sov. Phys. Usp.* **25**, 231 (1982).
22. Y. Murakami *et al.*, Resonant X-ray scattering from orbital ordering in $LaMnO_3$. *Phys. Rev. Lett.* **81**, 582 (1998).

23. J. D. Axe *et al*., Structural phase transformations and superconductivity in $La_{2-x}Ba_xCuO_4$. *Phys. Rev. Lett.* **62**, 2751–2754 (1989).
24. M. Fujita, H. Goka, K. Yamada, J. M. Tranquada, L. P. Regnault, Stripe order, depinning, and fluctuations in $La_{1.875}Ba_{0.125}CuO_4$ and $La_{1.875}Ba_{0.075}Sr_{0.050}CuO_4$. *Phys. Rev. B* **70**, 104517 (2004).
25. P. Santini *et al*., Multipolar interactions in *f*-electron systems: The paradigm of actinide dioxides. *Rev. Mod. Phys.* **81**, 807–863 (2009).
26. M. S. Ikeda *et al*., Ac elastocaloric effect as a probe for thermodynamic signatures of continuous phase transitions. *Rev. Sci. Instrum.* **90**, 083902 (2019).
27. Y. S. Li *et al*., Elastocaloric determination of the phase diagram of Sr_2RuO_4. *Nature* **607**, 276–280 (2022).
28. M. S. Ikeda *et al*., Elastocaloric signature of nematic fluctuations. *Proc. Natl. Acad. Sci. U.S.A.* **118**, e2105911118 (2021).
29. P. Gegenwart, Grüneisen parameter studies on heavy fermion quantum criticality. *Rep. Prog. Phys.* **79**, 114502 (2016).
30. L. Squillante, I. F. Mello, A. C. Seridonio, M. de Souza, Elastocaloric-effect-induced adiabatic magnetization in paramagnetic salts due to the mutual interactions. *Sci. Rep.* **11**, 1–10 (2021).
31. H. Yamauchi, T. Osakabe, M. Kosaka, E. Matsuoka, H. Onodera, High-pressure studies of DyB_2C_2. *J. Korean Phys. Soc.* **62**, 2084–2087 (2013).
32. D. Jayalakshmi, E. Viswanathan, M. Sundareswari, D. Hemanand, Theoretical investigation of thermoelectric property and damage tolerance of LuB_2C_2 compound. *Comput. Condens. Matter* **28**, e00566 (2021).
33. U. Staub *et al*., Orbital dynamics of the 4*f* shell in DyB_2C_2. *Phys. Rev. Lett.* **94**, 036408 (2005).
34. Y. Tanaka *et al*., Evidence of antiferroquadrupolar ordering of DyB_2C_2. *J. Phys. Condens. Matter* **11**, L505 (1999).
35. O. Zaharko, W. Sikora, F. Bialas, U. Staub, T. Nakamura, Quadrupolar, structural, and magnetic ordering in DyB_2C_2 studied by symmetry analysis and neutron diffraction. *Phys. Rev. B* **69**, 224417 (2004).
36. L. Ye *et al*., Data for Manuscript "Elastocaloric signatures of symmetric and antisymmetric strain-tuning of quadrupolar and magnetic phases in DyB2C2". Stanford Digital Repository. https://doi.org/10.25740/wy533np2837. Deposited 1 August 2023.
37. L. Testardi, Elastic modulus, thermal expansion, and specific heat at a phase transition. *Phys. Rev. B* **12**, 3849 (1975).
38. E. Du Tremolet de Lacheisserie, D. Gignoux, M. Schlenker, eds., *Magnetism: I. Fundamentals* (Springer, New York, NY, 2002).
39. R. M. Fernandes, J. Schmalian, Manifestations of nematic degrees of freedom in the magnetic, elastic, and superconducting properties of the iron pnictides. *Supercond. Sci. Technol.* **25**, 084005 (2012).
40. J. M. Bartlett *et al*., Relationship between transport anisotropy and nematicity in FeSe. *Phys. Rev. X* **11**, 021038 (2021).
41. A. Little *et al*., Three-state nematicity in the triangular lattice antiferromagnet $Fe_1/3NbS_2$. *Nat. Mater.* **19**, 1062–1067 (2020).
42. A. Hubert, R. Schäfer, *Magnetic Domains: The Analysis of Magnetic Microstructures* (Springer Science & Business Media, 2008).
43. T. Yanagisawa *et al*., Dilatometric measurements and multipole ordering in DyB_2C_2 and HoB_2C_2. *J. Phys. Soc. Jpn.* **74**, 1666–1669 (2005).
44. G. Gehring, K. Gehring, Co-operative Jahn–Teller effects. *Rep. Prog. Phys.* **38**, 1 (1975).
45. J. Ziman, Antiferromagnetism by the Bethe method. *Proc. Phys. Soc. A* **64**, 1108 (1951).
46. A. Beath, D. Ryan, Fcc antiferromagnetic Ising model in a uniform external field solved by mean-field theory. *Phys. Rev. B* **72**, 014455 (2005).
47. E. Fradkin, S. A. Kivelson, M. J. Lawler, J. P. Eisenstein, A. P. Mackenzie, Nematic fermi fluids in condensed matter physics. *Annu. Rev. Condens. Matter Phys.* **1**, 153–178 (2010).